Geothermics 115 (2023) 102805

Contents lists available at ScienceDirect

Geothermics

journal homepage: www.elsevier.com/locate/geothermics

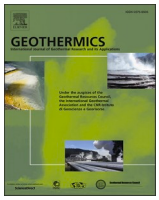

Hydraulic injection tests in the pilot EGS borehole PVGT-LT1 in Litoměřice, Czechia

T. Fischer [a,*], J. Vlček [a,c], P. Dědeček [b], J. Řihošek [d], G. Zimmermann [e], J. Holeček [d], M. Mazanec [a,c], L. Rukavičková [d], L. Janků [a], E. Káldy [a]

[a] Faculty of Science, Charles University, Prague, Czechia
[b] Institute of Geophysics, Academy of Sciences of the Czech Republic, Prague, Czechia
[c] Institute of Rock Structure and Mechanics, Academy of Sciences, Prague, Czechia
[d] Czech Geological Survey, Prague, Czechia
[e] Helmholtz Centre Potsdam GFZ German Research Centre for Geosciences, Germany

ARTICLE INFO

Keywords:
Geothermal energy
Hydraulic injection
Seismic monitoring
Stress field

ABSTRACT

Successful utilization of geothermal energy is conditioned by sufficient permeability of the rock formation as a heat exchanger. We present results of hydraulic injection tests carried out in 2020 in the pilot geothermal borehole PVGT-LT1 in Litoměřice, Czech Republic, which samples 800 m of Paleozoic and Mesozoic sediments on the top of a crystalline basement. The low hydraulic conductivity on the order of 10^{-11} m/s obtained by recovery tests was verified by large-scale injection tests monitored by DTS temperature logging. During the first test, 24 m^3 of water were injected and a permeable fracture was created at 880 m depth, breaking through the ignimbrite layer. The opening pressure of 12.55 MPa corresponds to the lower estimate of the minimum stress at this depth. The second injection was performed 7 months later and 202 m^3 were injected at flow rates reaching 50 l/min. It showed that the fracture had been preserved since the first injection, which was documented by a non-zero flow rate at the smallest injection pressures and also by a stabilized water level in the borehole, which dropped immediately after the fracture formation. No induced seismicity accompanied the injection, which indicates a possibly low seismogenic potential of this area of the Bohemian Massif. The model of finite conductive fracture fitted to the pressure decay curve during shut-in intervals gives an estimate of a fracture half-length exceeding 100 m.

1. Introduction

Areas of active hydrothermal systems that can be used for power production have been known and developed for decades (e.g. Larderello in Italy or Wairakei in New Zealand). However, high subsurface temperatures and groundwater flow sufficient to support such systems are not evenly distributed all over the world, although the actual energy demand and popularity of renewable energy resources, including geothermal energy recognized as a high-potential heating and power source, is growing. There are many mid-temperature regions with a large potential for creating EGS (Enhanced Geothermal System) worldwide. A pilot project in Soultz-sous-Forets (France), which started in 1986, has shown ways to address challenges in development of deep underground heat exchangers and improve their performance (Genter et al., 2009). This project was followed in the same setting of Rhine Graben on German-French border with other projects like Rittershoffen (France), Insheim and Landau (Germany), but also many other at different places - e.g. Habanero and Paralana, Australia, and The Geysers, Desert Park and Newberry, USA (Lu, 2018).

Different setups of hydraulic tests are used to identify hydraulic parameters of reservoir rocks. Usually, wells are stimulated by large amounts of water (several hundreds to thousands of cubic meters) (Baisch et al., 2002; Hofmann et al., 2019; Kwiatek et al., 2010) and seismicity is used to monitor the reservoir behavior (Baria et al., 1999). It is important to observe and test hydraulic performance and long-term circulation parameters (Schill et al., 2017) to ensure reservoir sustainability. In the Czech Republic, geothermal energy utilization is limited to shallow resources used for heating, aided by heat pumps (Dědeček et al., 2016). The first project for deep geothermal energy was commenced in Litoměřice, where a pilot geothermal borehole PVGT-LT1 was drilled

* Corresponding author.
E-mail address: fischer@natur.cuni.cz (T. Fischer).

https://doi.org/10.1016/j.geothermics.2023.102805
Received 19 May 2023; Received in revised form 8 July 2023; Accepted 10 August 2023
Available online 30 August 2023

between November 2006 and July 2007 (Šafanda et al., 2020). It reached a depth of 2111.2 m and its upper section of 215.9 mm diameter was completed with 162 mm ID casing and cemented down to 852.2 m. The remaining part of the borehole is uncased (Fig. 1a). The deviation of the bottom section from vertical ranges from 1.5 to 5.8°. Detailed description of drilling methodology and technical parameters of the borehole are summarized in the final report by Myslil et al. (2007). Technical problems occurred during the attempt to collect core samples from the final depth of 2111.2 m, which resulted in swelling of graphite-bearing shale and wellbore failure, so that the borehole collapsed below 1825 m and is inaccessible to the final drilled depth. Production tubing of 73 mm OD was installed down to 1800.5 m and perforated in the bottom part to test for circulation of hot water (Šafanda et al., 2020). This tubing was removed in 2019 and the open hole section was cleaned down to the depth of 1630 m. The deeper parts of the borehole (2111–900 m) are composed of relatively homogeneous garnet-kyanite mica-schists locally alternated with greenschists and graphitic phyllites at depths below ~1790 m. These rocks are overlain by altered and tectonically disrupted rhyolite ignimbrites (900 to 780 m), upper-Carboniferous continental siliciclastic sediments (780 to 190 m) and a sedimentary cover of sandstones and marlstones of the Bohemian Cretaceous Basin. Detailed descriptions of the lithology, geology and physical parameters of the rocks are given in Šafanda et al. (2020 and 2023). The caliper log and acoustic borehole televiewer (BHTV) logs show strong cavitation at the depth interval from the casing shoe down to 1140 m (Fig. 1b), which corresponds to the volcanic rocks and underlying fractured zone of mica-schists (Fig. 1c). Below, only thin fractures are documented in the logs (Procházka and Kořalka, 2018).

Well PVGT-LT1 penetrates a confined fractured-rock aquifer at the depth of 852.2 to 2111.2 m and the wellhead pressure reached 79 kPa prior to commencement of hydraulic tests. After opening the well head, groundwater flowed freely over the casing rim. The overflow was small, on the order of less than tens of milliliters per minute (~20 ml/min), and inversely proportional to the ambient atmospheric pressure. The source of the groundwater was at least at the depth of 852 m, which corresponds to the location of the casing shoe. The water is of NaCl character with 11 g/l of total dissolved solids. Currently, after the hydraulic tests performed in 2020, the hydraulic head is 21.1 m below ground level (160.5 m above reference sea level).

In this paper, we present the results of hydraulic test performed in the well PVGT-LT1 with the aim to evaluate hydraulic properties of the rock mass at natural conditions and at high water pressures. To this purpose, recovery tests followed by two large scale injection tests were carried out to identify and characterize the main flow zones intersected by the well PGVT-LT1. The experiments were accompanied by seismic monitoring using a dense surface seismic network to assess the potential for triggering induced seismicity by the high-pressure water flow.

2. Measurements and data analysis

2.1. Recovery tests

It was not practical to conduct a standard pumping test in low permeability formations encountered in the well. To estimate the transmissivity of the rock before extraction of the production steel tubing, cleaning of the borehole and hydraulic tests, two recovery tests were performed in August 2018 and August 2019. For this purpose, the water level in the borehole was decreased by ~38 m via one day of pumping before the first recovery test, and by ~9.3 m by two hours long pumping before the second recovery test. Water level recovery was monitored using a pressure logger (Solinst Levelogger) lowered down the borehole until the water level reached the well head, which took 47 h in the case of the first recovery test and 40 h in the case of the second recovery test. The measured water level data were barometrically compensated before further processing. The Theis (1935) recovery method was used to determine the transmissivity of the formation.

2.2. Injection tests

2.2.1. First hydraulic test, January 2020

The hydraulic program of the first large scale injection test was carried out in the period 24 – 27 January 2020. Water was injected to the borehole using a flange welded to the wellhead cover. A frequency-controlled pump was used with the maximum design pressure of 40 bar. A tank with 38 m^3 of river water at a temperature of 5°C was used as a water source. A datalogger with an integrated pump control was connected to a laptop PC for online monitoring of the flow rate and pressure; a sampling interval of 1 min was used, which was decreased to 10 s and 1 s for specific time intervals. Further injection and data acquisition parameters are shown in Table 1.

Fig. 2a shows the pressure and flow rate curves for the whole injection period. After the initial tests of the equipment, the first long-term injection program with pressure steps of 32, 36 and 40 bar started 24 January, 18:00. The very low permeability of the formation manifested

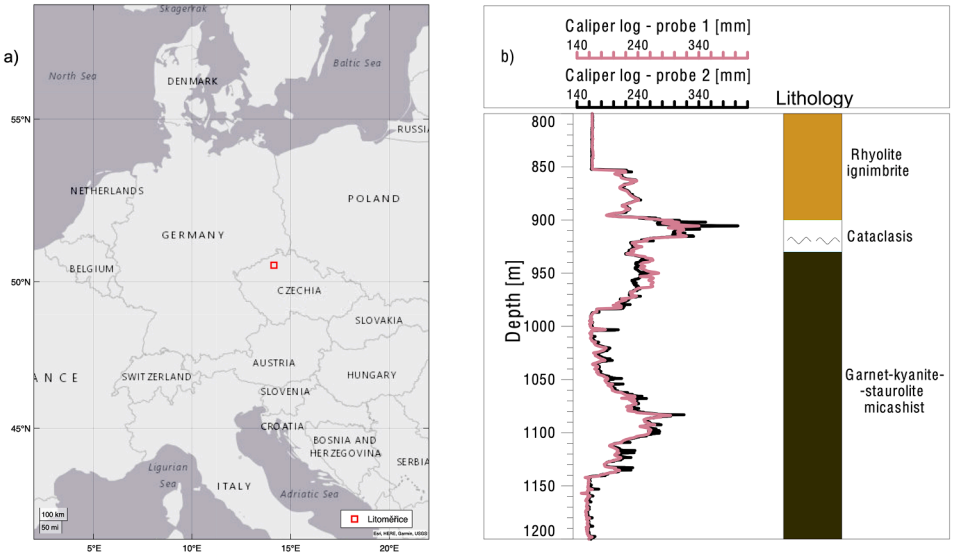

Fig. 1. (a) Map showing position of the Litoměřice area. (b) On the left: cavity log showing a disrupted zone under the casing shoe at 852.2 m, measurements are color coded for 2 different caliper probes. On the right: corresponding lithological description.

Table 1
Characteristics of the pump and the data acquisition for the first and second injection experiment

	Pump parameters		Data acquisition				
Dates in 2020	Maximum pressure (bar)	Min-Max flow rate (l/min)	Sampling interval (s)	Pressure	Flow rate	Backflow rate	Total volume
24 Jan – 27 Jan	41	3.5 – 45	60, 10, 1 (end of injection)	Datalogger @ 60, 10 and 1 s intervals		Analog flowmeter	
31 Aug – 06 Sep	100	2-170	1, 15 (after shut-in)	Datalogger @ 1 s intervals		Digital flowmeter	

itself in a very low average flow rate of 0.1 l/min, which decreased with time due to the saturation of the formation. The low flow rate was achieved by pump cycles caused by setting an upper pressure limit, which resulted in short injection pulses. After 13.5 h of injection, we increased the pressure limit to 36 bar and again after 3.5 h to 40 bar. The flow rate stayed, however very low, not exceeding 0.5 l/min. After the next 5 h, we increased the pressure to 41 bar, which resulted in an immediate flow increase to 11 l/min and a pressure drop indicating a fracture formation. This is illustrated in Fig. 3 showing that a fracture formed and opened immediately after the first pressure pulse exceeded 40 bar. Then a slow pressure decay and a flow rate increase followed, reaching 18 L/min.

Next, from 25 January, 20:00 until 26 January, 18:00, three injection stages were carried out at flow rates of 7, 13 and 21 l/min. Note that the frequency-controlled pump did not allow for precise control of the flow rate, which resulted in a varying flow rate depending on the fracture impedance. During some of the stages, the flow and pressure are inversely correlated, which is caused by manual handling of the valve or by changing the pump frequency to keep the flow constant. Despite these variations, the pressure shows a slow increase with the increasing flow rate and does not exceed the fracture opening pressure of 40.5 bar. The experiment was terminated by a pressure decay test of 2 h duration followed by opening the wellhead on 26 January, 22:00. During the injection, three additional pressure decay tests were carried out to gather data for estimation of the fracture transmissivity and its development with injection. In total, 24.3 m^3 of water were injected and 5.3 m^3 flowed back after opening of the borehole at the end of the experiment.

2.2.2. *Second hydraulic test, September 2020*

The second test was based on the results of the first experiment. This injection was made in the period 31 August – 5 September 2020 using a grouting pump with maximum design pressure of 100 bar and maximum flow rate of 170 l/min. The construction of the pump allowed control of

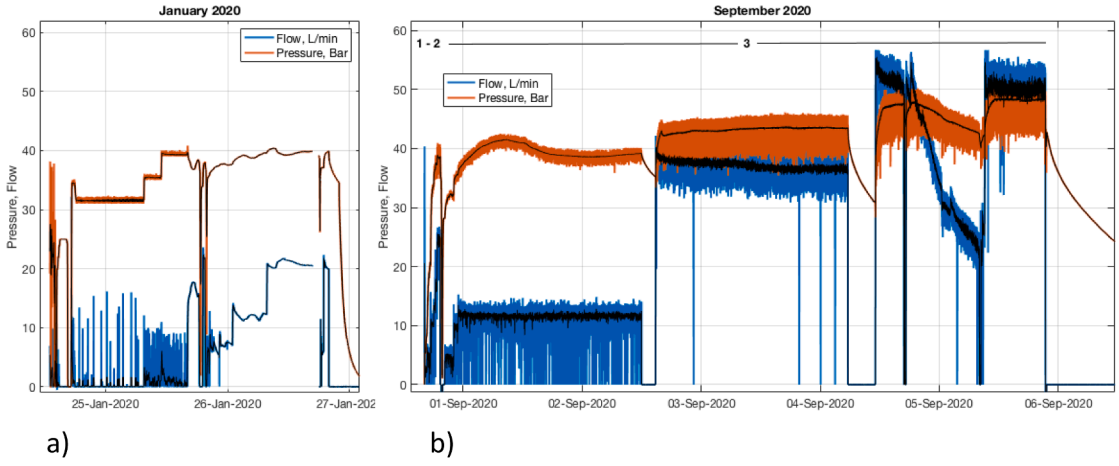

Fig. 2. Injection history of the January 2020 (a) and August-September 2020 (b) experiment. Black lines show a running average over 10 points. The pulses of flow during the first half of the January 2020 experiment at low flow rates are due to the interrupted injection when the pressure reached the 40-bar limit. A data gap on 26 January between 16:44 and 18:00 was caused by a malfunction of the data recorder. Negative flow rates are not shown. Stages of the August-September 2020 experiment are shown by numbers 1, 2, and 3 at the top of the (b) diagram.

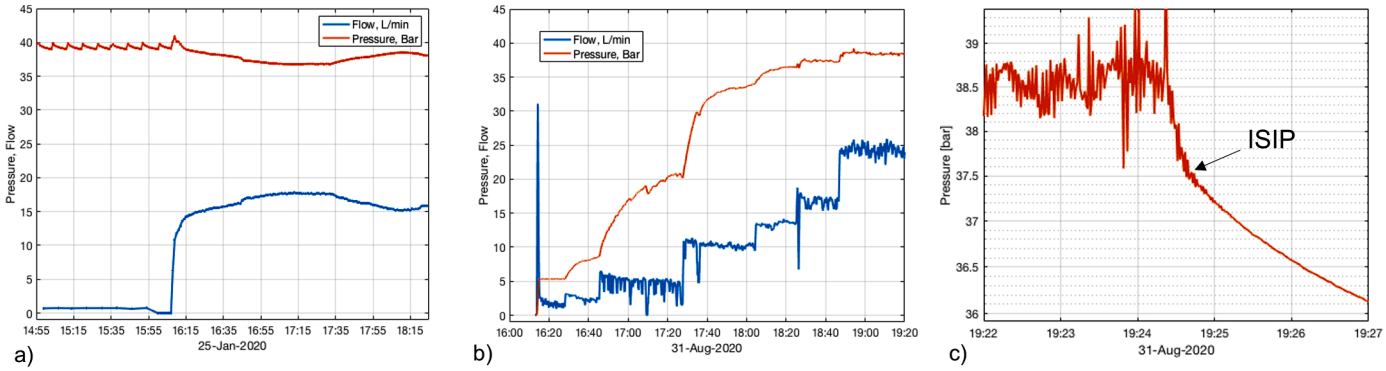

Fig. 3. Flow and pressure during fracture opening in January 2020 (a), and September 2020 (b) – stags 1 and 2 from Fig. 2b and during shut-in in September 2020 (c) where the instantaneous shut-in pressure estimate (ISIP) is indicated. The same period of 3.5 h is shown in (a) and (b).

the flow rate based on the frequency of the piston strokes. The pump was connected to the wellhead using high-pressure hydraulic hoses and water at a temperature of 15°C was taken directly from the water supply. Data quality was controlled by real-time plotting onsite.

This experiment consisted of three stages (Fig. 2b). First, it was verified whether the fracture, which was formed during the first experiment of January 2020 stayed open until August 2020. To address this, water was injected into the well at a rate of 2 l/min. After filling the well with water, the pressure stabilized at 5 bar (Fig. 3b), a much lower pressure than the 40.5 bar required for creating the fracture in January (Fig. 3a). This confirmed that after 7 months since the first injection, the fracture had not healed and remained at least partially open.

In the second stage, a short-term stepwise injection was carried out to assess the borehole injectivity. Water was injected at a series of 7 flow rates of 2.3, 4.4, 9.9, 13.5, 16.4 and 23.5 l/min for a period of 10 to 30 min, with each step maintained until the pressure stabilized.

The main stage of this experiment was a large-scale injection consisting of three injection periods at 12, 38 and 50 l/min, with each step lasting about 36 h. Instability of the pump occurred during this phase, which resulted in a pressure loss and a flow rate decay for a period of about 14 h. After terminating each injection period, bleed-off was carried out.

The final injection period terminated accidentally when the pressure hose was punctured resulting in uncontrolled leakage of water for 11 min, and a pressure loss from 48 to 42 bar. The borehole was then closed, and a pressure decay test of 4 days duration followed, which was terminated by opening the borehole. During this experiment, 202.5 m^3 of water were injected in total and 2.8 m^3 of water flowed back after opening the borehole at the end of the experiment. This small volume of backflow, compared to the first experiment, is probably caused by the much longer duration of the pressure decay test at the end of the second experiment compared to the first one.

The trends of the pressure vs flow rate for both the experiments differ significantly (Fig. 3a and b). An abrupt increase of flow rate is apparent in the first (January 2020) experiment, when the flow rate increased from fractions of l/min to more than 10 l/min after fracture creation. Then, with increasing flow rates, the pressure stayed almost constant, not exceeding 40 bar. On the contrary, during the second (August-September 2020) experiment, the water pressure increase followed an increase in flow rate until the pressure approached 35 bar. Then, only a small pressure increase followed the continuing flow rate increase indicating the fracture had opened.

2.3. Temperature monitoring

A Distributed Temperature Sensing (DTS) system was used to monitor the temperature and water flow along the borehole. It consisted of fiber optic cable armored with stainless steel loose tube suspended in the borehole down to a depth of 1700 m and a Sentinel unit (Sensornet Ltd) in a single-ended configuration. System calibration was ensured using an isothermal box equipped with precise temperature sensors, which was placed between the borehole and the device and contained 20 m of coiled optical fiber. As a second calibration point, we used the temperature at a depth of 1650 m, which was measured during previous temperature logging. The DTS system allowed repeated measurement along the entire length of the well at pre-set time intervals, with measurement accuracy increasing with time interval length. For both hydraulic experiments, a time interval of 30 min was chosen, which was temporarily shortened to 10 min in the case of expected dynamic temperature changes. The spatial resolution was set at 1 m. The optical cable was installed into the borehole just before the first hydraulic test, and therefore it was possible to measure both during the campaigns and the relaxation of the borehole in the following months.

The temperature field of both injections (Fig. 4) shows an abrupt

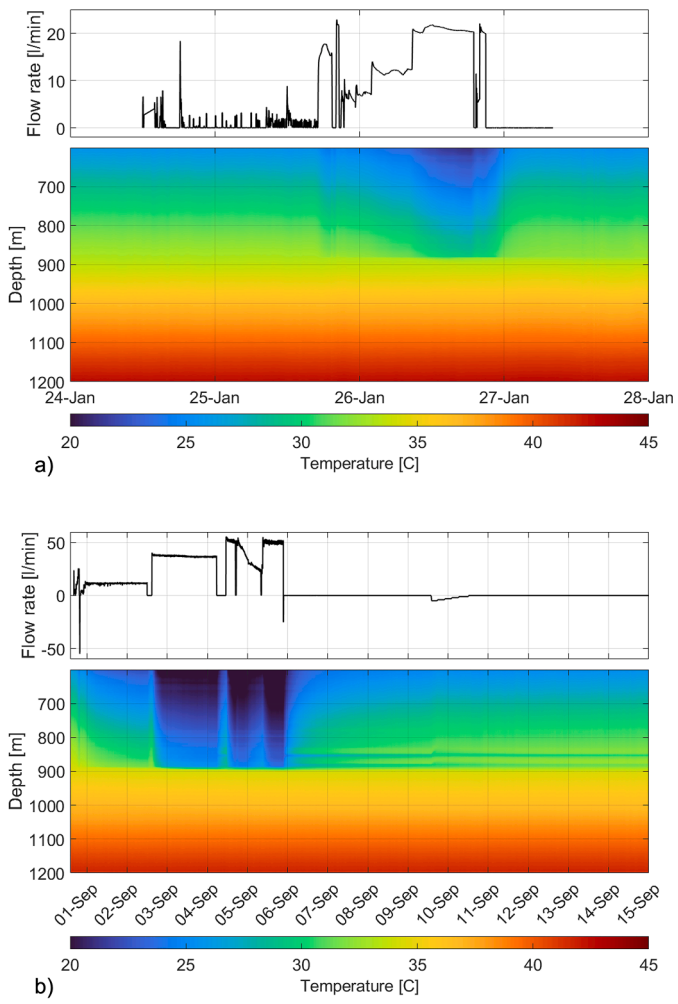

Fig. 4. Flow rate (upper panels, smoothed with running average) and temperature map (bottom panels) for the first – January 2020 (a) and for the second – August/September 2020 (b) injection tests. In January 2020 backflow was not measured.

temperature increase (color changes from blue to yellow) with depth at 880 m pointing to water leakage at this depth. This indicates that a fracture was formed here, extending approximately from 880 to 885 m depth. The temperature bellow 890 m depth remained unchanged during the tests.

2.4. Seismic monitoring

The area of the Litoměřice geothermal project is monitored by a permanent seismic network consisting of six surface broadband (BB) or short-period (SP) 3-component stations operational since 2019, and four 6-component stations of the rotaphone type (Brokešová and Málek, 2013). In June 2020, the network was expanded with a broadband borehole station (GLT2) located in a 200 m deep well at the distance of 85 m from the pilot well PVGT-LT1. During the January 2020 experiment, a temporary network of twenty SP stations was deployed to enhance the detection sensitivity of monitoring. For the second hydraulic test in August-September 2020, only four of these temporary stations were deployed in addition to the permanent network (Fig. 5). The permanent network provides a magnitude of completeness of –0.6 at 2 km depth (Káldy and Fischer, 2023).

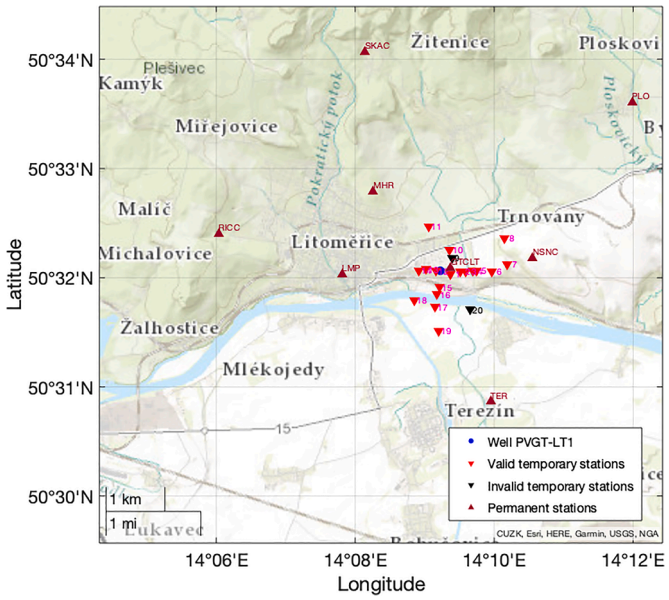

Fig. 5. Map of a temporary dense network of seismic stations (red) installed for the first hydraulic treatment in January (no data recorded at black stations). Only stations no. 5, 11, 14 and 19 were installed temporarily for the second injection in August and September. Additionally, you can find permanent seismic stations (cyan) and the pilot well PVGT-LT1 (blue point). (For interpretation of the references to colour in this figure legend, the reader is referred to the web version of this article.)

3. Results and interpretation

3.1. Hydraulic parameters

Transmissivities $K{\cdot}h$ of $6{\cdot}10^{-9}$ m^2/s and of $2.5{\cdot}10^{-9}$ m^2/s were derived from the two recovery tests performed before extraction of the tubing, well cleaning and conducting the pressure tests which could affect the natural hydraulic properties of formation. Such transmissivities indicate impermeable conditions. Due to degassing of water in the borehole during pumping, it was not possible to conduct proper pumping tests. Thus, the transmissivities evaluated by recovery tests are only indicative of the in-situ conditions. The water level during the recovery test can also be affected by movement of gas bubbles (methane produced by biogenic activity from carboxymethyl cellulose in the drilling fluid) present on the surface of borehole walls. The bubbles can cause ambiguity of water level readings at the end of the recovery period. Since the shorter period of pumping before the second recovery test led to underestimated values of transmissivity, we consider the value of the first recovery test to be more credible. We estimated the hydraulic conductivity K for the expected conductive zones from the first recovery test to be between $4.77{\cdot}10^{-12}$ m/s and $6.00{\cdot}10^{-11}$ m/s, depending on the length of the expected conductive zone (see Table 2).

Hydraulic conductivity acquired from recovery tests can be compared with hydraulic conductivities of samples extracted from the core samples. These samples are composed mainly of garnet mica-schist with quartz bands up to 1 cm thick. The samples represent unfractured rock from depths of 992.3 m, 980.5-980.8 m and 984.7-984.9 m. Because these samples lack fractures, their laboratory-acquired hydraulic conductivities are 2 to 4 orders lower than the hydraulic conductivities obtained from the recovery tests (Table 3).

Table 2
Hydraulic conductivity of the permeable part of the borehole according to the first recovery test

Conductive interval	Length h [m]	K [m/s]	Note
852 – 2111 m	1259	$4.77{\cdot}10^{-12}$	Open hole interval
852 – 1250 m	398	$1.51{\cdot}10^{-11}$	Lower rock resistivity interval
852 – 1100 m	~100	$6.00{\cdot}10^{-11}$	Caverning intervals

3.2. Temperature field and the fracture

The time evolution of the temperature field (Fig. 4) is shown in more detail in Fig. 6. The rapid temperature increase at 880 m depth demonstrates a major fluid loss into a fracture that formed during the January 2020 experiment and was reopened during the August-September 2020 experiment. The temperature drop in the interval above the fracture was significantly smaller during the January 2020 injection (Fig. 6a) than during the August-September 2020 one (Fig. 6c). This is due both to the lower flow rate and the shorter duration of the January 2020 test. Also note the local minimum of the temperature at depths from 50 to 400 m during the August-September 2020 injection caused by the relatively warm water injected, compared to the January 2020 injection. Temperatures after shut-in, when the fracture closed, and warming of the water above the fracture can be seen in Fig. 6b and d. In both cases, the increase in temperature was relatively fast and was influenced mainly by the backflow of water from the borehole. In January 2020 (Fig. 6b), the borehole remained closed for two hours after the end of the tests, and only conductive heat transfer occurred. After opening of the borehole and the subsequent backflow, the warming rate was accelerated due to convection. This is clearly seen in Fig. 6b, where this faster warming causes a gap between the temperature curves measured at 2 and 3 h after the end of the tests. Similarly, in August-September 2020 (Fig. 6d), when the well was opened at 21:30 on the 5 September 2020, a significant increase in temperature followed due to convective heat transfer. Interestingly, in contrast to the January 2020 experiment, there are two temperature minima found during the September 2020 temperature recovery (Fig. 6d). We will discuss the possible origin of the temperature minima at 853 and 880 m depth below.

3.3. Induced seismicity

During the first and second hydraulic experiments, a Pepin automatic event detector and locator (Fischer, 2003, 2022) operated in near real time on seismic data from the permanent seismic network (GRSN). As no induced microearthquakes were detected, the data corresponding to the first experiment were carefully inspected in detail with special focus on the interval following 25-Jan-2020 15:00 UTC when the pressure and flow records showed that a fracture was created. Data from the 6 permanent and 18 temporary stations were examined but no seismic events were detected in this case either. Although Fig. 7a displays a number of seismic bursts, they do not coincide among stations, which points to their local character.

In an attempt to detect even very weak seismic activity we applied a source scanning algorithm (Kao and Shan, 2004; Vlček et al., 2016; Fischer et al., 2020; Lávička and Fischer 2022) to the data from all 24 available seismic stations. For this purpose, we shifted the seismograms back in time using time delays corresponding to the travel times from

Table 3
Hydraulic conductivities of rock samples from laboratory tests. Foliation dip indicates orientation of foliation relative to flow direction.

Sample	Sampling depth [m]	Foliation dip [°]	K [m/s]
LIT 1/1	992.3	2	$4.54{\cdot}10^{-15}$
LIT 2/1	980.5-980.8	15	$1.51{\cdot}10^{-15}$
LIT 2/2	980.5-980.8	80	$1.18{\cdot}10^{-15}$
LIT 2/3	980.5-980.8	5	$1.06{\cdot}10^{-14}$
LIT 3/1	984.7-984.9	80	$8.09{\cdot}10^{-15}$
LIT 3/3	984.7-984.9	3	$1.29{\cdot}10^{-15}$

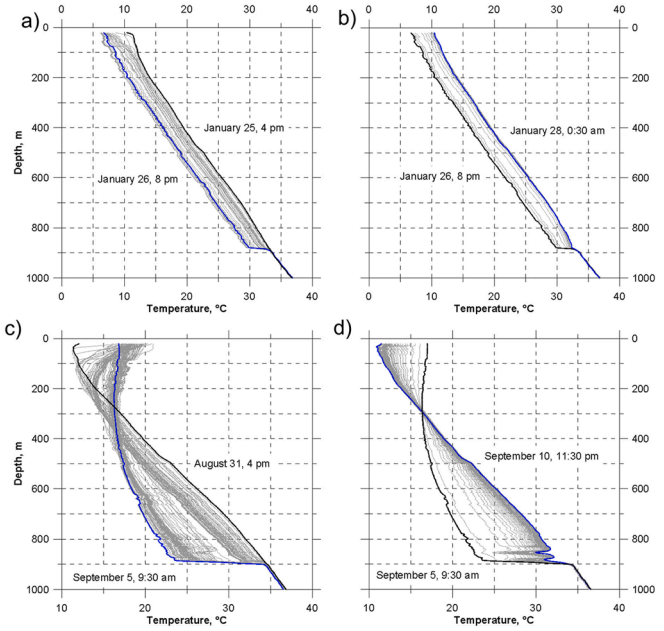

Fig. 6. Development of subsurface temperature in one-hour steps during both campaigns. The figures on the left (a,c) show the temperature change during water injection, on the right (b,d) the following period of relaxation of the borehole after the end of the tests is shown. The time interval between the grey temperature curves is 1 h.

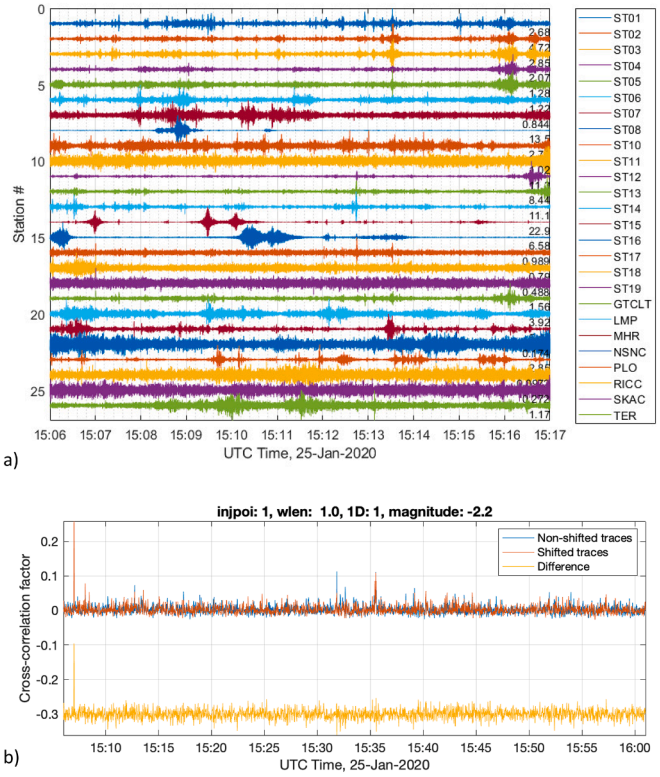

Fig. 7. (a) Vertical components of all available temporary and permanent seismic stations for the time period of 11 min including the formation time of hydraulic fracture in the PVGT-LT1 borehole (25 January 2020, at about 15:10). Additionally, to assess the detection capability of the cross-correlation detector, seismograms of a weak M_L = -2.2 synthetic event originated at 15:07 in the location of the fracture were added to the seismograms. Note a tiny spike at 15:07 occurring at some seismic stations.
(b) One hour interval of multi-channel correlation of all traces with no time shift (blue) and with time shift corresponding to the synthetic event location (red); their difference (yellow) is shifted by -0.3 to avoid the overlap of traces. (For interpretation of the references to colour in this figure legend, the reader is referred to the web version of this article.)

the examined hypocentre to individual stations; a 1D velocity model was used to this purpose. We benefited from the fact that the fracture was formed in the close vicinity of the well and so we used only a single location of the hypocentre in the borehole, at the depth of the fracture, and examined a time interval of 1 h after the fracture opened. We searched for a correlated signal on the station seismograms by cross correlating the envelopes of the seismogram's vertical component in a moving window. The choice of the seismogram envelope instead of the original seismogram was motivated by our aim to detect not only a brittle fracture but also noise tremors. These tremors could be generated by water flow in the fracture (Umlauft and Korn, 2019), which could have opened aseismically.

The multichannel cross-correlation was carried out in the following way. Assuming **X** is a matrix with n columns equal to seismogram envelopes at individual stations, we computed cross-correlation factors between all its columns. This resulted in a n x n matrix **Y** composed of cross-correlation factors between all pairs of station seismogram envelopes. Finally, the multi-channel cross-correlation factor was obtained as the mean value of the **Y** elements. A moving window of 1 s length shifted by 0.5 s was used to compute the cross-correlation factors. The possible detections were identified by comparing the cross-correlation of original traces (blue trace in Fig. 7b) and those shifted by the travel times from the expected hypocentre (red trace in Fig. 7b); the difference is shown by the yellow trace in Fig. 7b.

To test the detection capability of this approach, we generated a synthetic event at the expected location of the fracture, whose origin was at 15:07, three minutes before the fracture formed. The amplitude of a sinc wavelet was scaled according to the decay curve used in the magnitude formula applied at GRSN (Káldy and Fischer, 2023) and its arrival time was computed using the applied 1D velocity model. The resulting pulse was added to the recorded seismograms with varying magnitude to assess the smallest detectable event. In this way we found that the cross-correlation detector can identify a synthetic microseismic event with a M_L magnitude as low as –2.5, depending on the seismic noise (see the pronounced peak of the cross-correlation factor at 15:07 in Fig. 7b of a M_L -2.2 event). On the other hand, no other peak of cross-corelation is found in the period 1h after fracture formation, which indicates that no induced seismic event with magnitude above ~-2.2 occurred.

3.4. Fracture location, stress field and well injectivity

As no induced seismicity, which could provide data on the fracture depth, extent and orientation, was detected, the fracture location can be constrained only by temperature monitoring in the borehole. The temperature logs show (Fig. 6) that the fracture formed at a depth of 880 m, only 30 m below the casing shoe. At the stress increases with depth, this shallow depth is most favorable for fracture creation. This depth interval is characterized by unstable borehole walls with cavities reaching double the borehole diameter (Fig. 1). Comparison with the lithology log shows that the fracture occurred in the 100 m thick layer of ignimbrite.

The acoustic borehole televiewer (BHTV) logs acquired 4 months before injection show that two steep fractures intersect the well at 880.5 and 890 m depth. Repeated BHTV measurements failed to provide a reproducible borehole wall image, which was probably caused by large cavities and roughness of the borehole wall. Accordingly, it was not possible to check the state of the two fractures after the injection tests. The temperature log modelling indicates that only a single fracture was opened in this depth interval; most likely it was the upper one whose depth closely fits the depth of the temperature drop.

We use the injection pressure record during fracture closure to

measure the normal stress acting on the fracture walls to estimate the minimum stress components σ_{min}. For this purpose, we used the first shut-in of 31 August 2020 at 19:24, which was made after injecting 2.2 m^3 of water. This volume was small enough to neglect far-field fracture closure. At a pressure of 37.5 bar, the pressure curve (Fig. 3c) shows a kink, which is typical of fracture closure and corresponds to the instantaneous shut-in pressure (ISIP) (Cornet, 2015). Adding the hydrostatic pressure at 880 m depth results in an opening pore pressure, p_{open}, of 125.5 bar. Because of the low flow rate of only 12 l/min, we neglect the viscous pressure losses. As the BHTV log showed different preexisting fractures in the borehole wall, we assume that the activated fracture was arbitrarily oriented and could fail either by shearing or tensile opening. As follows from the stress analysis (Fischer and Guest, 2011; Cornet, 2015), the pressure p_s required for shear failure is smaller than the pressure p_t required for tensile opening, which equals σ_{min}, $p_s < p_t = \sigma_{min}$. Here, depending on the fracture type, p_{open} corresponds either to p_s *or* p_t. Therefore, the pore pressure p_{open} at which the fracture was activated corresponds to the lower estimate of the minimum stress, i.e. $\sigma_{min} > 125.5$ bar. The resulting linear gradient with depth z is given by $\sigma_{min} > 14.3\ z$ [km], which is quite similar to the stress gradient obtained at Soultz-sous-Forets of $\sigma_{min} = -1.7 + 14.07\ z$ (Valley and Evans, 2007). The similarity of the σ_{min} gradient at Soultz-sous-Forets with its lower estimate in Litoměřice confirms the realism of our measurement. For comparison, the minimum horizontal stress at KTB is 25 MPa at 880 m depth (Brudy et al., 1997), which is double of the lower estimate of σ_{min} at Litoměřice.

In both experiments, a step test was carried out to characterize the formation behavior at different water pressures. For this purpose, water pressure and flow rate were measured for each step after their values stabilized. This way, six data points were obtained for each experiment. Additionally, three data points were measured during the long-term January 2020 experiment (Fig. 8). Different pressure-flow relation is apparent. During the January 2020 test, flow rate was negligible at pressures exceeding 30 bar, whereas in the August-September 2020 test, the pressure built up almost linearly with increasing flow rate, until the pressure exceeded 36 bar. Then, a rapid flow rate increase occurs with only a small pressure increase. This indicates a different behavior of the fracture. For pressures below 36 bar, a linear behavior is observed with the injectivity of about 0.03 l/min/bar. At higher pressures, the injectivity rises by one order to about 3.9 l/min/bar (0.65 l/s/MPa). For economic operations, much larger injectivities on the order of 10 l/s/MPa would be needed (e.g. Baria et al., 1999). The two pressure intervals with different pressure gradients correspond to two modes of fracture flow. At low pressures, the fracture existed but stayed closed, and water used the existing permeability along the rough fracture walls, resulting in a linear relationship between pressure and flow rate. When the water pressure exceeded the normal stress on the fracture, the fracture has opened, and its conductivity significantly increased (Cornet 2015; Hofmann et al., 2019).

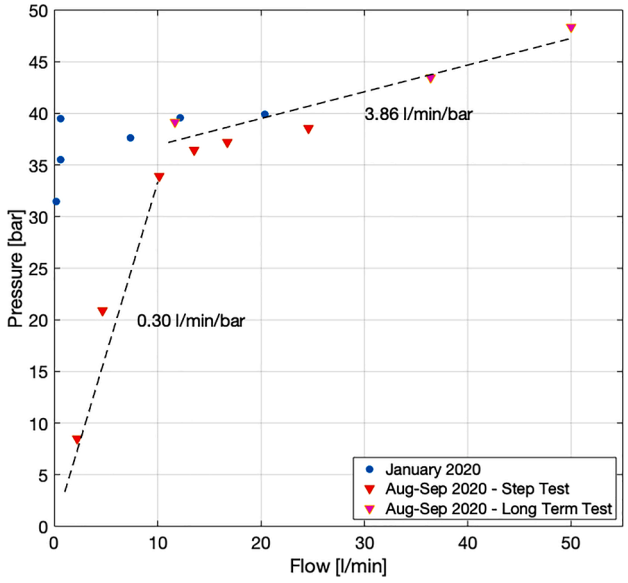

Fig. 8. Pressure and flow rates during the step injection test for the January (blue circles) and August-September 2020 (red triangles) experiment. The dashed lines show injectivity of 0.3 l/min/bar (0.05 l/s/MPa) and 3.9 l/min/bar (0.65 l/s/MPa) corresponding to two pressure intervals during the September tests. For $p < 36$ bar the fracture stays closed but permeable and for $p > 36$ bar the fracture gets open.

3.5. Fracture flow characteristics

We used the model of a finite conductive fracture in a homogeneous infinite reservoir (Fig. 9) to estimate the fracture and reservoir parameters (according to Cinco-Ley and Samaniego, 1981). Different fracture flow and reservoir flow characteristics were tested by pressure matching of the various model combinations with the software Saphir - Pressure Transient Analysis (KAPPA Engineering).

The fall-off sequences (shut-in periods) and flowback (production periods) during and after the stimulation treatment were analyzed using classical well test analysis procedures of Horne (1995). The evolution of transmissivity and permeability of the reservoir rock is thus calculated from pressure decline curves after each injection stage, considering the superposition principle and assuming infinite-acting radial flow. The calculations are based on the generalized formula for pressure (p) development with stepwise flow rate (q) changes (Lee, 1982). During the first and second injection experiments, a total of 7 pressure decay tests were performed and four of them were found suitable for characterization of the fracture parameters (Fig. 10). More details on theoretical background and the formulas used for the analyses are shown and described in the Appendix.

We analyzed one fall-off (shut-in) sequence from January 2020 and 3 fall-off sequences from August-September 2020 (Table 4). The durations of these four shut-in intervals were 2.0, 2.8, 5.6 and 88.5 h. Pressure matching led to the same models for all intervals. Best fits were achieved with a finite conductive fracture with homogeneous reservoir conditions and no boundaries (infinite extension of model). The vertical length (pay zone) was set to 100 m according to Table 2 and with respect to the caverning intervals in the depth section from 852 to 1100 m. The related porosity is 10 % and was used in all models. Dynamic viscosity of the injected fluid was set to ambient conditions (0.001 Pa·s).

The transmissivity of the first test in January 2020 is $3.4 \cdot 10^{-15}$ m^3 (3.4 mDm) with a calculated fracture half-length of 101 m (Table 4). Transmissivity (k x h) of the first two tests in August-September 2020 is 2.3 mDm ($2.3 \cdot 10^{-15}$ m^3) and 3.3 mDm, which are much shorter than the third interval. For the third interval, transmissivity is 38 mDm and therefore ten times higher. The half-length of the fracture shows a different result. The length increases from 103 m to 136 m for the first two intervals, but then decreases to 18.1 m for the last interval. Taking into consideration that before shut-in, there was a leakage through a punctured hose, and hence a production rate of 70 l/min with a pressure release for about 11 minutes, it is very likely that the fracture was starting to close in the far field and only the adjacent part was still open. A further closing of the fracture continued during the long-term shut-in period of 88 h. The same behavior is apparent for fracture conductivity - the longer the shut-in, the lower the fracture conductivity is. This can be associated with a closure over time.

As the height of the inflow zone is not known (only transmissivity can be obtained from the analysis), we tested the sensitivity of the inversion results to the pay zone height, which is related to the overall rock permeability. The influence is shown in Table 5 for the 3rd shut-in in September 2020 with pay zones of 20,50, and 100 m. The dependence of fracture half-length and fracture conductivity varies according to the

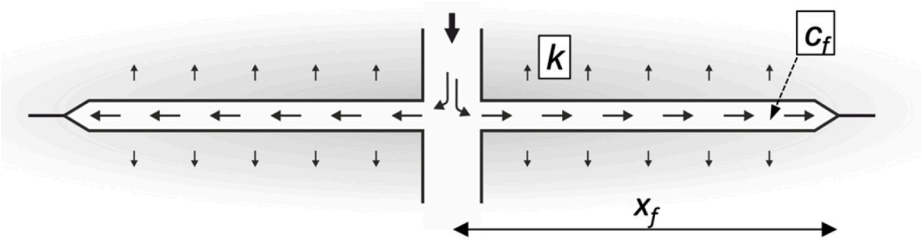

Fig. 9. Model of the finite conductive fracture in homogeneous rock environment. Formation permeability k, fracture conductivity c_f and its half-length x_f are indicated.

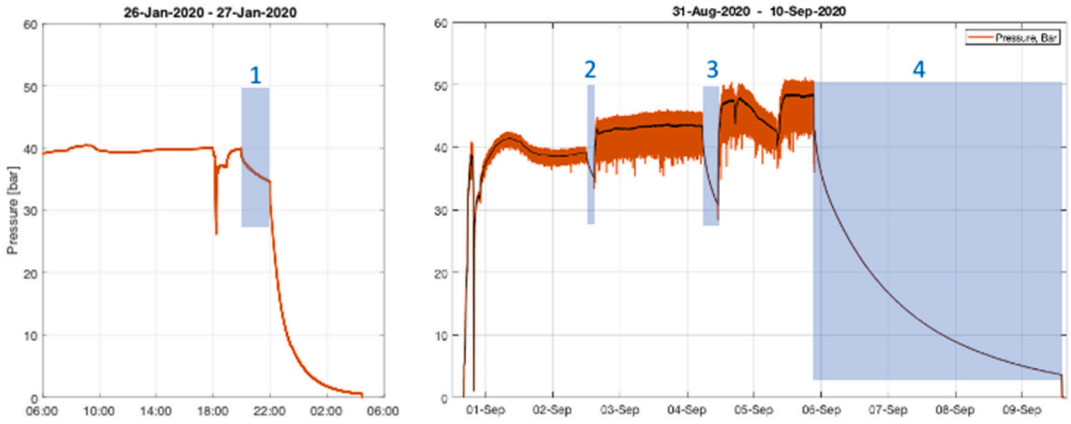

Fig. 10. Shut-in intervals used for the pressure decay tests for determination of the fracture characteristics.

Table 4
Results of the well test analysis of the last shut-in interval during the January 2020 campaign and the 3 shut-in intervals during the injection test in September 2020

	shut-in January 2020	shut-in 1 August-September 2020	shut-in 2 September 2020	shut-in 3 September 2020
Model	Well: fracture - Finite Conductivity Reservoir: Homogeneous boundary: Infinite			
Duration [h]	2.05	2.84	5.64	88.5
Volume injected prior to shut-in [m^3]	24	29	115	203
Pay zone h [m]	100	100	100	100
Permeability k [m^2]	$3.43{\cdot}10^{-17}$	$2.26{\cdot}10^{-17}$	$3.30{\cdot}10^{-17}$	$3.80{\cdot}10^{-16}$
Transmissivity k x h [m^3]	$3.43{\cdot}10^{-15}$	$2.26{\cdot}10^{-15}$	$3.30{\cdot}10^{-15}$	$3.8{\cdot}10^{-14}$
Frac. half-length x_f, [m]	101	103	136	18.1
Frac. conductivity k_f x b_f [m^3]	$1.82{\cdot}10^{-13}$	$2.95{\cdot}10^{-12}$	$2.85{\cdot}10^{-13}$	$1.32{\cdot}10^{-14}$

Table 5
Fracture parameters for different pay zones

Model	Well: fracture - Finite Conductivity Reservoir: Homogeneous boundary: Infinite		
pay zone h [m]	20	50	100
Transmissivity k x h [m^3]	$3.8{\cdot}10^{-14}$	$3.8{\cdot}10^{-14}$	$3.8{\cdot}10^{-14}$
fracture half-length x_f [m]	40.4	25.5	18.1
fracture conductivity k_f x b_f[m^3]	$4.16{\cdot}10^{-16}$	$1.64{\cdot}10^{-15}$	$4.65{\cdot}10^{-15}$
permeability [m^2]	$1.9{\cdot}10^{-15}$	$7.6{\cdot}10^{-16}$	$3.8{\cdot}10^{-16}$

model equations (see Appendix), since rock permeability is changing with pay zone height (transmissivity is constant).

4. Discussion

The January 2020 large scale injection experiment was designed with the aim of characterizing the hydraulic parameters of the formation targeted by the PVGT-LT1 borehole and to verify at large pressures the low permeability found during the laboratory measurements of the rock samples and during the recovery tests. For this purpose, a temperature profile was measured continuously using a DTS cable. It was expected that distributed flow zones would be identified as discontinuities in the temperature profile. During the step test, only very low permeability was found, manifested by low flow rates in fractions of l/min for well-head pressures up to 40 bar (Figs. 2a and 4a). Once the pressure exceeded 40 bar, the flow rate abruptly increased, and the pressure slowly decreased showing a formation of new volume. The origin of this behavior becomes apparent in the real-time temperature monitoring – the whole temperature profile continuously decreased only above a depth of 880 m, showing leakage of water at this depth (Fig. 4a and 6a). This was interpreted to be the result of fracture creation and its growth. After injecting 24 m^3 of water with flow rates up to 20 l/min, the 2-day injection test was terminated, and borehole was shut-in. After 2 h it was opened and the pressure was allowed to bleed-off what was reflected by a fast temperature recovery (Figs. 4a and 6b).

In August-September 2020, the experiment was repeated to examine the formation response during long-term injection at higher flow rates. A similar behavior was found. Based on the temperature log, water leaked only at 880 m depth. Flow rates up to 50 l/min were reached at wellhead pressures up to 48 bar.

During the August-September campaign, in contrast to only one

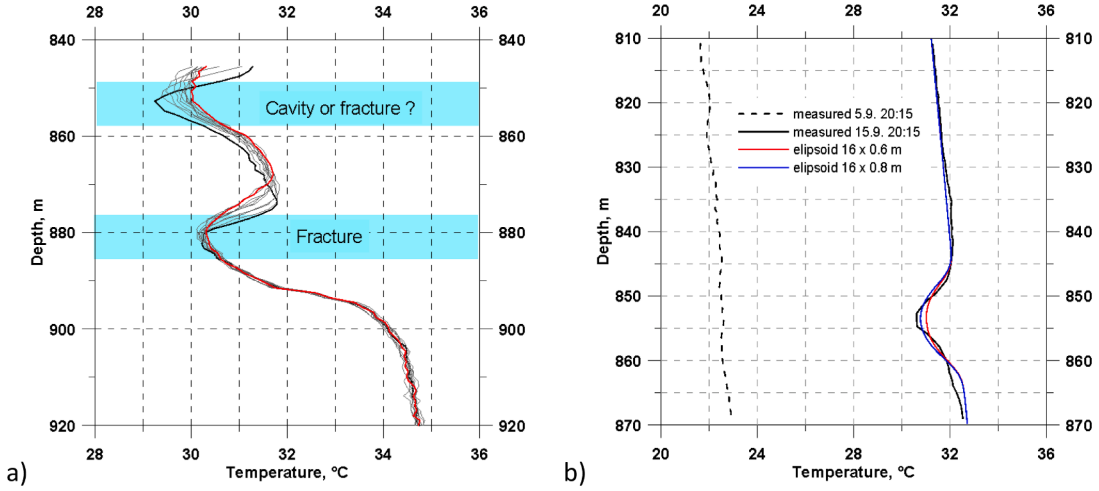

Fig. 11. (a) Detailed view of the temperature anomalies in the borehole during the water backflow; the black and red curves correspond to 9 September 2020, 14:15 and 15:55, respectively; the curves interval is 10 min.
(b) Comparison of the measured temperature anomaly at 853 m depth with simulated anomalies modelled by cavities of ellipsoidal shape. The dashed black line shows the initial temperature profile in the time of shut-in on 5 September, 20:30; the full lines show the measured (black) and modelled (blue and red) temperature profiles.

minimum in the winter experiment, two temperature minima formed after shut-in as the temperature recovered (Fig. 6d). While the deeper minimum at 880 m corresponds to the fracture formed in the winter experiment, the shallower minimum at a depth of 853 m is just below the casing shoe. This temperature anomaly looks very similar to the one at a depth of 880 m, which was caused by cooling of the rock around the open fracture. Therefore, the question arises whether another fracture could have formed during the hydraulic tests. To shed light on the origin of the shallower temperature minimum, we show (Fig. 11a) a detailed temperature log measured after bleeding the borehole on 9 September 2020. The 880 m minimum shows a slight temperature drop with time and almost neglectable shift of the minimum upwards caused by the backflow of cold water from the fracture. In contrast, the 853 m temperature minimum shifts upwards in the direction of water flow much more significantly (about 2 m), and the temperature increases by 0.8°C due to the heat that the water brought from the greater depths. The larger changes of the upper minimum compared to the lower one are consistent with the cumulative influence of backflow from the 880 m fracture and the possible fracture at 853 m depth. In this sense, also the upper temperature minimum can be caused by an open fracture. On the other hand, any open fracture should be manifested during injection by a fluid loss, which would be reflected as an abrupt temperature drop at the depth of the inferred fracture, similar to what we observe at 880 m. However, the temperature curve is continuous around the depth of 853 m during injection (Fig. 4b, 6c), which rules out the existence of an open fracture at 853 m.

Another possible source of the temperature minimum at 853 m could be an accumulation of cold water in a cavity that would, due to its symmetrical shape, keep its low temperature longer than a thin borehole. The caliper logs (Fig. 1) show large cavities in the well between the depth of 850 and 1150 m, which are still expanding, according to the repeated measurements in 2007 and 2019. To verify this hypothesis, we numerically modelled warming of the borehole containing an ellipsoidal cavity that would fit the observed temperature curve ten days after shut-in (Fig. 11b). The simple conductive numerical model of an ellipsoidal cavity neglects natural convection in the borehole, which would likely have accelerated the warming process. The optimal model indicates a cavity 16 × 0.8 m (blue curve in Fig. 11b) in size.

One of the aims of the injection experiments was to examine the seismic response of the rock volume to water injection. It turned out that despite creating a fracture at a depth of 880 m, no microearthquakes were induced by injection during either of the two experiments. The ISIP wellhead pressure of 37.5 bar corresponds to fracture opening pressure of 125.5 bar. This represents, in the case that the fracture was a new tensile fracture, the minimum stress component σ_{min}. If the existing fracture was sheared, 125.5 bar is the lower estimate of the minimum stress component σ_{min}. Higher σ_{min} than its lower estimate is expected in the more likely case of shearing a preexisting fracture, which occurs at lower injections pressures, before the pressure reaches σ_{min}. Shear failure is also consistent with the fact that the 880 m fracture retained its permeability after the pressure drop (Pine and Batchelor, 1984; Cornet, 1987; Baria et al., 1999). Without knowing the fracture geometry and the direction of the principal stress in the area this ambiguity cannot be resolved with certainty.

The aseismic character of the fracture formation in an otherwise impermeable medium provides valuable information on the seismogenic character of the area. Even using a densified seismic network, no microseismic event was detected. If any seismic event occurred, its radiated energy was too small, below the detection sensitivity of the seismic monitoring. According to Káldy and Fischer (2023) the minimum detectable magnitude is -1 at 1 km depth. However, our tests using a synthetic event and a cross-correlation based detector indicated a microearthquake down to M_L -2.5 could be detected when noise bursts are absent. (Fig. 7). The seismic monitoring sensitivity however varies with seismic noise; the fracture occurred on a working day, around 4 p. m. local time in the suburbs of an urban area with dense car and train traffic nearby. These factors can hide very small events, which would occur contemporaneously with noise bursts.

In general, injection-induced seismicity is not generated in under-critically stressed rocks. These occur if the differential stress is not high enough so that the additional pore pressure does not suffice to exceed the Coulomb failure stress. This is the case at shallow depths where the differential stress is small (Zoback, 2007) or in regions with missing tectonic load. This is probably the case of the intracontinental regions like the 9.4 km deep KTB borehole in Germany (Jost et al., 1998; Baisch et al., 2002) or geothermal borehole in Gross Schoenebeck (Kwiatek et al., 2010) where only M_L<1 and M_L<-1 microearthquakes, respectively, were induced by massive water injections. Both conditions are met in our experiment, which took place in less than 1 km depth in the stable environment of Bohemian Massif.

Successful fracture creation was also demonstrated by a change of the hydrogeological regime of the PVGT-LT1 borehole after the injection

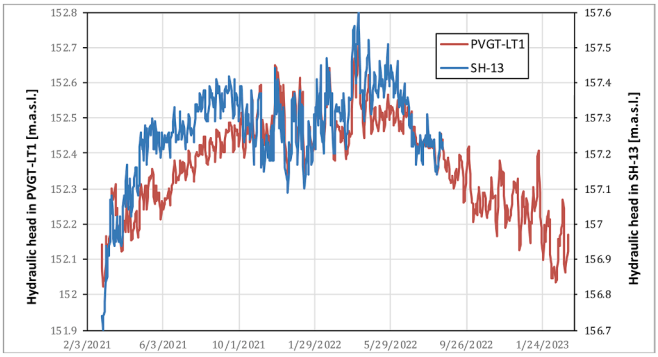

Fig. 12. Hydraulic head trend in boreholes PVGT-LT1 and SH-13. Time series of hydraulic head in PVGT-LT1 with fracture developed at the base of Carboniferous formation shows identical short-term variations and similar trend as hydraulic head in SH-13 within the Cenomanian aquifer.

experiments. Prior to the first large scale injection test in January 2020, the hydraulic head was 8.1 m above ground surface (181.6 m a.s.l.). After fracture formation in January 2020 the hydraulic head dropped and after the September 2020 injection its level stabilized 21.1 m below the ground surface (160.5 m a.s.l.). This level remained constant so far, indicating that the fracture is, after three years, still permeable. The new hydraulic head corresponds to the Cenomanian aquifer in the vicinity of Litoměřice and to the upper part of the less permeable underlying Carboniferous aquifer, which are both influenced by the Elbe River in the vicinity of Litoměřice (Krásný et al., 2012).

To understand the character of the hydraulic connection formed by fracture creation we compared the groundwater level variations in the PVGT-LT1 borehole with those in the SH-13 borehole (Fig. 12), which is located about 4.5 km to ENE in Velký Újezd. The hydraulic head in PVGT-LT1 is approximately 4.9 m lower than in SH-13 and short-term variations in the water level and their trend are similar in both boreholes. This indicates that the fracture has connected the borehole to the Cenomanian aquifer. This connection would require fracture propagation upwards. Considering the location of the open interval within the Cenomanian aquifer of the Bohemian Cretaceous Basin between 57 and 14 m.a.s.l. (165 to 190 m below surface) and a fracture intersection with the borehole at 880 m depth, the depth difference is about 690 m. This is much greater than the modelled fracture half-length of about 130 m (Table 4). Alternatively, the fracture could have intersected a permeable zone in a Carboniferous formation that is hydraulically connected with Cenomanian.

The fracture model was developed from well test analyses by fitting the pressure curve and the related pressure derivative function. The most likely model was a finite conductive fracture with a limited fracture half-length together with an infinite acting radial flow in the far field. In addition, based on the pressure curves at later stages, no boundary conditions could be observed. These results are supported by temperature logs showing a clear indication of a fractured inflow zone generated during the hydraulic stimulation of the well.

5. Conclusions

We conducted several experiments to characterize the hydraulic properties of metamorphic rocks encountered in a 2.1 km deep pilot geothermal borehole PVGT-LT1 in Litoměřice, Czechia. Two recovery tests showed low transmissivities on the order of 10^{-9} m^2/s, which implies a hydraulic conductivity on the order of 10^{-11} m/s. Comparison with hydraulic conductivity of the rock samples in the order of 10^{-15} m/s indicates the dominating role of fractures in controlling fluid flow.

The large-scale injection tests performed along the whole well length confirmed the low permeability of the formation which abruptly increased when the wellhead pressure exceeded 40 bars. The depth of water leakage was identified using a temperature log measured by a DTS fiber optic cable at 880 m, only 30 m below the casing shoe. The fracture of unknown geometry was formed in a 100 m thick ignimbrite layer.

After a 7-month long break, a similar injection test was performed. In total 202 m^3 were injected, significantly more than 24 m^3 during the first test. The higher flow rate at low pressures indicated the fracture remained partially open since its creation. The pressure at which the fracture activated was estimated to be 125.5 bar, which corresponds to the lower estimate of the minimum stress. Borehole injectivity exhibits two extreme values. For wellhead pressures below 36 bar, when the fracture was closed, the injectivity was 0.05 l/s/MPa. When wellhead pressure exceeded 36 bars, the injectivity rose to 0.65 l/s/MPa.

No induced seismicity was detected by a dense seismic network during either injection experiment, which made it impossible to estimate the fracture geometry. We attribute the aseismic behavior to the shallow depth of the fracture and possibly also small seismogenic potential of the area where no natural microearthquake has been recorded so far. We estimated the fracture size by matching the pressure decay curve during shut-in intervals to theoretical predictions for a finite conductive fracture in an infinite medium. A fracture conductivity of 10^{-13} to 10^{-12} m^3 and a half-length exceeding 100 m was estimated. Interestingly, the water level dropped by 29 m after the fracture creation and its temporal variations have been similar to those of a shallow aquifer. This indicates a breakthrough of the fracture upwards. Further activities towards development of an EGS reservoir in this site should focus on drilling a new borehole doublet, and on the identification of a more permeable fracture system that could be stimulated to achieve economic flow rates.

CRediT authorship contribution statement

T. Fischer: Conceptualization, Methodology, Software, Investigation, Formal analysis, Writing – original draft, Visualization, Supervision, Project administration, Funding acquisition. **J. Vlček:** Software, Investigation, Data curation, Formal analysis, Writing – original draft, Visualization. **P. Dědeček:** Methodology, Investigation, Data curation, Formal analysis, Writing – original draft, Visualization. **J. Řihošek:** Investigation, Formal analysis, Writing – original draft, Visualization. **G. Zimmermann:** Methodology, Investigation, Formal analysis, Writing – original draft. **J. Holeček:** Formal analysis, Writing – original draft. **M. Mazanec:** Investigation. **L. Rukavičková:** Investigation. **L. Janků:** Writing – review & editing. **E. Káldy:** Formal analysis.

Declaration of Competing Interest

No conflict of interests of the author and coauthors was identified.

Data availability

Data will be made available on request to the corresponding author.

Acknowledgments

Our deepest gratitude goes to Francois Cornet, who provided valuable advice for the design and running of the first injection experiment. We would also like to thank the Czech Hydrometeorological Institute, especially Anna Lamačová for providing us with water level data of monitored boreholes. We also acknowledge Antonín Tym for his help with arranging the experiments. The research was supported by the RINGEN - research infrastructure upgrade “No CZ.02.1.01/0.0/0.0/16_013/0001792, co-funded by the EU Operational Programme Research, Development and Education”.

Appendix

The evolution of transmissivity and permeability is calculated from pressure decline curves after each injection stage taking into account the superposition principle and assuming infinite acting radial flow (e.g. Horne, 1995). The calculations are based on the generalized formula for pressure development with stepwise flow rate changes:

$$p(t) = p_0 + \sum_{i=1}^{n} \frac{(q_i - q_{i-1})\mu}{4\ \pi\ k\ h}\left(0,5772 + ln\left(\frac{\Phi\mu c_t r^2}{4k(t - t_{i-1})}\right) - 2s\right)$$

with $p(t)$ = well pressure; p_0 = initial pressure; h = interval length (height of reservoir); k = rock permeability; q_i = flow rate at i-th interval; μ = dynamic viscosity of fluid; t_i = interval time i; t = total time; Φ = porosity; c_t = total compressibility; r = well radius; s = skin (set to zero)

Transmissivity

Transmissivity ($k{\cdot}h$) is calculated from the pressure derivative function assuming infinite acting radial flow (IARF) (e.g. Horne 1995)

$$\frac{\partial(p_0 - p(t))}{\partial\left(\ln\ t/t + t_{inj}\right)} = \frac{q\ \mu}{4\ \pi k\ h}$$

with q = flow rate; t_{inj} = total injection time; t = duration of fall-off time (shut-in time).

There are two different definitions of transmissivity in literature. One is the product of hydraulic conductivity K (in m/s) and the pay zone height h (in m) resulting in a transmissivity ($K{\cdot}h$) in m^2/s. The other is the product of permeability k (in m^2) and pay zone height h (in m) resulting in a transmissivity ($k{\cdot}h$) in m^3. The conversion from hydraulic conductivity to permeability is the following: $K = k{\cdot}\rho{\cdot}g/\mu$, with ρ = water density, g = gravitational acceleration, μ = dynamic viscosity of water. Under ambient conditions the conversion factor is: 1000 kg/m^3 · 9,81 m/s^2 / 0,001 Pa·s = 10^7 1/(m·s).

Fracture flow of a finite conductive fracture (bi-linear flow)

Pressure changes during fracture flow through a finite conductive fracture exhibit a fourth root time dependence (according to Cinco-Ley and Samaniego, 1981):

$$\Delta p = \frac{q\ B\ \mu}{2\Gamma\left(\frac{5}{4}\right)\ h}\left(\frac{t}{4\ k\ \left(k_f\ b_f\right)^2 \mu\ \Phi\ c_t}\right)^{0.25} \sim\ t^{0.25}$$

with

k_f = fracture permeability; b_f = fracture aperture; ($k_f\ b_f$) = fracture conductivity; B = Formation factor (set to 1); Γ = Gamma function

Fracture half-length

The fracture half-length is obtained by time matching of the transition from bi-linear flow behavior to infinite acting radial flow.

References

Baisch, S., Bohnhoff, M., Ceranna, L., Tu, Y., Harjes, H.P., 2002. Probing the crust to 9-km depth: fluid-injection experiments and induced seismicity at the KTB superdeep drilling hole, Germany. Bull. Seismol. Soc. Am. 92 (6), 2369–2380.

Baria, R., Baumgärtner, J., Rummel, F., Pine, R.J., Sato, Y., 1999. HDR/HWR reservoirs: concepts, understanding and creation. Geothermics 28, 533–552.

Brokešová, J., Málek, J., 2013. Rotaphone, a self-calibrated six-degree-of-freedom seismic sensor and its strong-motion records. Seismol. Res. Lett. 84 (5), 737–744.

Brudy, M., Zoback, M.D., Fuchs, K., Rummel, F., Baumgärtner, J., 1997. Estimation of the complete stress tensor to 8 km depth in the KTB scientific drill holes: Implications for crustal strength. J. Geophys. Res. Solid Earth 102 (B8), 18453–18475.

Cinco-Ley, H., Samaniego-V, F., 1981. Transient pressure analysis for fractured wells. J. Pet. Technol. 1749–1766.

Cornet, F.H., 1987. Results from Le Mayet de Montagne project. Geothermics 16 (4), 355–374.

Cornet, F.H., 2015. Elements of Crustal Geomechanics. Cambridge University Press.

Dědeček P., Šafanda J., and Tym A. Geothermal energy use, country update for the Czech republic.

Fischer, T., 2003. Automatic location of swarm earthquakes from local network data. Stud. Geophys. Geod. 47 (1), 83–98.

Fischer, T., Guest, A., 2011. Shear and tensile earthquakes caused by fluid injection. Geophys. Res. Lett. 38, L05307. https://doi.org/10.1029/2010GL045447.

Fischer, T., Hrubcová, P., Salama, A., Doubravová, J., Ágústsdóttir, T., Gudnason, E.Á., Hersir, G.P., 2022. Swarm seismicity illuminates stress transfer prior to the 2021 Fagradalsfjall eruption in Iceland. Earth Planet. Sci. Lett. 594, 117685.

Fischer, T., Kühn, D., Roth, M., 2020. Microseismic events on the Åknes rockslide in Norway located by a back-projection approach. J. Seismolog. 24 (1), 55–74. https://doi.org/10.1007/s10950-019-09884-5.

Genter, A., Fritsch, D., Cuenot, N., Baumgartner, J., Graff, J., 2009. Overview of the current activities of the European EGS Soultz project: from exploration to electricity production. Proceedings Thirty-Fourth Workshop On Geothermal Reservoir Engineering. Stanford University, Stanford, California. February 9-11, 2009, SGP-TR-187.

Hofmann, H., Zimmermann, G., Farkas, M., Huenges, E., Zang, A., Leonhardt, M., Kim, K. Y., 2019. First field application of cyclic soft stimulation at the Pohang Enhanced geothermal system site in Korea. Geophys. J. Int. 217 (2), 926–949. https://doi.org/10.1093/gji/ggz058.

Horne, R.N., 1995. Modern Well Test Analysis, 926. Petroway Inc.

Jost, M.L., Büßelberg, T., Jost, Ö., Harjes, H.P., 1998. Source parameters of injection-induced microearthquakes at 9 km depth at the KTB deep drilling site, Germany. Bull. Seismol. Soc. Am. 88 (3), 815–832.

Káldy, E., Fischer, T., 2023. Microseismic network sensitivity in case of no seismic activity. Case study from Litoměřice in Czech Republic, proof-tested in West Bohemia. J. Seismolog. 27, 627–641. https://doi.org/10.1007/s10950-023-10134-y.

Kao, H., Shan, S.J., 2004. The source-scanning algorithm: Mapping the distribution of seismic sources in time and space. Geophys. J. Int. 157 (2), 589–594.

Krásný, J., Císlerová, M., Čurda, S., Datel, J., Dvořák, J., Grmela, A., Hrkal, Z., Kříž, H., Marszalek, H., Šantrůček, J., Šilar, J., 2012. Podzemní Vody České Republiky: Regionální Hydrogeologie Prostých A Minerálních Vod. Česká geologická služba, Praha, p. 1144. ISBN 978-80-7075-797-0.

Kwiatek, G., Bohnhoff, M., Dresen, G., Schulze, A., Schulte, T., Zimmermann, G., Huenges, E., 2010. Microseismicity induced during fluid-injection: A case study from the geothermal site at Groß Schönebeck, North German Basin. Acta Geophys. 58, 995–1020.

Lávička, V., Fischer, T., 2022. Rupturing of small natural earthquakes in West Bohemia investigated by source scanning. J. Seismolog. 26 (1), 57–78. https://doi.org/10.1007/s10950-021-10043-y.

Lee, J., 1982. Well testing. In: SPE Textbook Series, 1. Society of Petroleum Engineers, p. 159.
Lu, S.M., 2018. A global review of Enhanced geothermal system (EGS). Renewable Sustainable Energy Rev. 81, 2902–2921.
Myslil, V., Stibitz, M., Frydrych, V., Jiráková, H., Fritschová, L., Šafanda, J., Burda, J., Brož, K., Karous, M., Landa, I., Procházka, M., Gregor, P., Wolfbauer, J., Kalaš, P., Motlík, J., Alinče, Z., Spudil, J., Pechar, T., Mužák, J., Sciranková, L., 2007. Závěrečná zpráva o řešení projektu v program Trvalá prosperita MPO v roce 2006–2007. Ev.č. projektu: 2A-1TP1/043. Název projektu: Geotermální vrtné ověření struktury Litoměřice pro energetické využití. Final project report (in Czech), ZavZprVaVMPO_0803. Ministry of industry and trade, Prague. December 2007.
Pine, R.J., Batchelor, A.S., 1984. Downward migration of shearing in jointed rock during hydraulic injections. Int. J. Rock Mech. Min. Sci. Geomech. Abstr. 21, 249–263.
Procházka, M., Kořalka, S., 2018. Revisional Measurements in the PVGT/LT-1 Borehole (in Czech). Report on Geophysical Logging Measurements. Aquatest a.s., Prague, p. 29.
Schill, E., Genter, A., Cuenot, N., Kohl, T., 2017. Hydraulic performance history at the Soultz EGS reservoirs from stimulation and long-term circulation tests. Geothermics 70, 110–124.
Šafanda, J., Verner, K., Franěk, J., Peřestý, V., Holeček, J., Fischer, T., 2020. Geology and geothermal potential in the eastern flank of Eger Rift (Litoměřice area, Czech Republic). Geothermics 86, 101808.
Šafanda, J., Dědeček, P., Čermák, V., Uxa, T., 2023. Heat flow variations in 2 km deep borehole Litoměřice, Czechia. Geothermics 111, 102708. https://doi.org/10.1016/j.geothermics.2023.102708.
Theis, C.V., 1935. The relation between lowering of the piezometric surface and rate and duration of discharge of a well using groundwater storage. Trans. Am. Geophys. Union 16, 519–524.
Umlauft, J., Korn, M., 2019. 3-D fluid channel location from noise tremors using matched field processing. Geophys. J. Int. 219 (3), 1550–1561.
Valley, B., Evans, K.F., 2007. Stress state at Soultz-sous-Forêts to 5 km depth from wellbore failure and hydraulic observations. Proceedings, 32nd Workshop On Geothermal Reservoir Engineering. Stanford University, Stanford, California, pp. 17469–17481. January 22-24.
Vlček, J., Fischer, T., Vilhelm, J., 2016. Back-projection stacking of P-and S-waves to determine location and focal mechanism of microseismic events recorded by a surface array. Geophys. Prospect. 64 (6), 1428–1440. https://doi.org/10.1111/1365-2478.12349.
Zoback, M.D., 2007. Reservoir Geomechanics. Cambridge Univ. Press, Cambridge, U. K, p. 499.